

Engineering the Composition and Structure of Bimetallic Au–Cu Alloy Nanoparticles in Carbon Nanofibers: Self-Supported Electrode Materials for Electrocatalytic Water Splitting

Juan Wang,[†] Han Zhu,^{*,†,‡,§} Danni Yu,[†] JiaWei Chen,[†] JiaDong Chen,[†] Ming Zhang,[†] LiNa Wang,[†] and MingLiang Du^{*,†,‡}

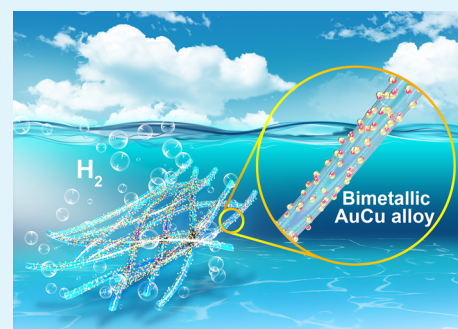
[†]College of Materials and Textiles, Key Laboratory of Advanced Textile Materials and Manufacturing Technology of the Ministry of Education, Zhejiang Sci-Tech University, Hangzhou 310018, P. R. China

[‡]School of Chemical and Material Engineering, Key Laboratory of Food Colloids and Biotechnology, Ministry of Education, Jiangnan University, Wuxi 214122, P. R. China

S Supporting Information

ABSTRACT: The bimetallic Au–Cu alloy nanoparticles have been constructed in electrospun carbon nanofibers (Au–Cu/CNFs), employing as high efficient hydrogen evolution reaction (HER) electrode. The morphology, structure, and composition of bimetallic Au–Cu alloy can be controlled by adjusting the precursor nanofibers through a facile approach. With the increased Cu content, the Au–Cu alloy have a transition from the homogeneous AuCu₃ alloy phase to the Au₃Cu phase with Cu shell. The self-supported bimetallic Au–Cu/CNFs hybrid can be directly employed as electrode materials for water splitting, and it showed excellent electrochemical activity, including long-term stability, high exchange current density, and low overpotential. The outstanding HER performance could be mainly attributed to the synergistic interactions and interfacial effects of Au–Cu alloy with high densities of uncoordinated surface atoms. In addition, the fast charge transport and the fast kinetic for the desorption of the gas were originated from the self-supported three-dimensional architectures consist of integrated Au–Cu/CNFs networks. The Au–Cu/CNFs with mass ratio of 1:2 (Au₃Cu–Cu “core-shell” alloy) obtain the lowest overpotential of 83 mV (at $j = 10 \text{ mA cm}^{-2}$), lowest Tafel slope of 70 mV dec^{-1} , and highest exchange current density of 0.790 mA cm^{-2} . The present investigations offer a new strategy for the design and synthesis of unique nanocrystals in energy conversion related application.

KEYWORDS: Au–Cu alloy, materials science, eletrospinning, electrocatalytic water splitting, hydrogen energy



INTRODUCTION

As highly efficient and sustainable clean energy source, molecular hydrogen (H₂) is expected to replace the fossil fuels to solve energy crises and environmental pollution.^{1,2} The electrocatalytic hydrogen evolution reaction (HER) is a promising method for producing hydrogen, and, however, the state-of-the-art noble metal electrocatalysts hinder its large-scale commercial applications due to their high cost and rarity as resources.^{3,4} Therefore, searching for a cost-effective and earth-abundant electrocatalysts with efficient HER performance is an urgent task.^{5,6} To solve this problem, a large number of transition metal compounds, such as molybdenum-, tungsten-, cobalt-, and nickel-based nanomaterials, have been widely reported as HER catalysts.^{7–10} Recently, Zhu et al. prepared a core–shell system containing cubic cobalt sulfide and layered molybdenum disulfide, and the core–shell nanostructure exhibited amazing electrochemical activity for both the HER and oxygen evolution reaction (OER), originating from the reduction of the kinetic energy barrier of H₂ desorption at the nanointerfaces between the Co₉S₈ and MoS₂ core–shell structures.¹¹ Kong et al. used carbon fiber papers to load

CoSe₂ NPs and measured their HER performance in a H₂SO₄ electrolyte.¹²

As a low-cost and earth-abundant 3d transition metal, the Cu metal possess excellent physical and chemical properties. However, although the Cu metal has been widely applied in many fields, it is rarely used as an electrocatalyst for the electrocatalytic water splitting.^{13–16} Recently, Xu et al. reported an ultrasmall Cu₇S₄@MoS₂ heteronanostructure in a donut shape with abundant active edge sites and possessing an overpotential of 113 mV at 10 mA cm⁻².¹⁷ Tran et al. synthesized a highly crystalline layered ternary Cu₂MoS₄ as a new efficient HER electrocatalyst with an onset potential of 135 mV.¹⁸ Jahan et al. prepared a composite based on Cu-centered metal organic framework and graphene oxide, using it as a trifunctional catalyst for HER, OER, and oxygen reduction reaction (ORR).¹⁹ Unfortunately, although enormous efforts have been made, the electrochemical performance and kinetic

Received: January 28, 2017

Accepted: May 26, 2017

Published: May 26, 2017

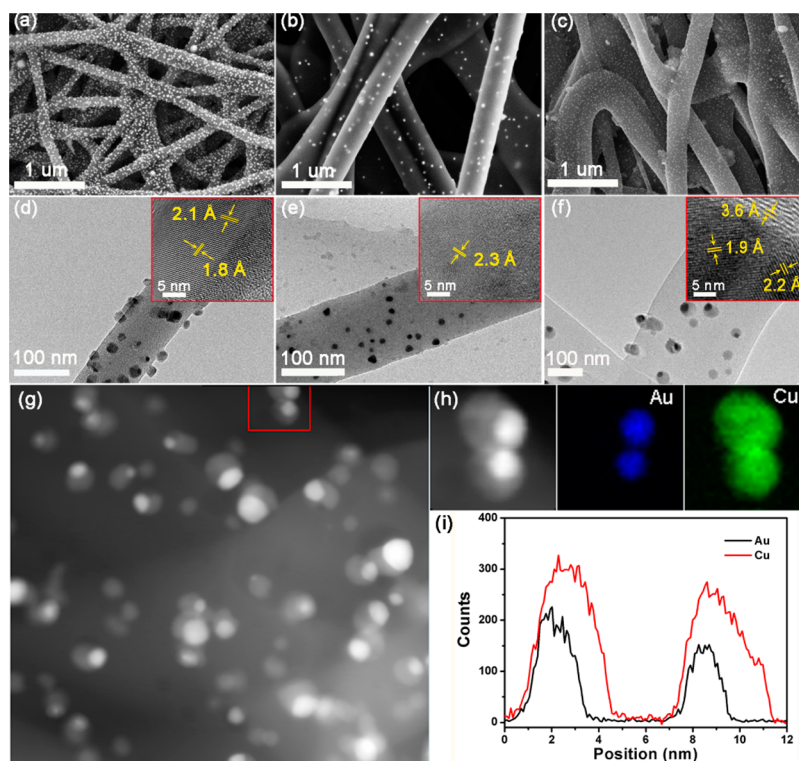


Figure 1. FE-SEM images of the (a) Cu/CNFs, (b) Au/CNFs, and (c) Au–Cu/CNFs. TEM image of (d) Cu/CNFs, (e) Au/CNFs, and (f) Au–Cu/CNFs, and the insets are the corresponding HRTEM images. (g) High-angle annular dark field STEM and (h) STEM energy dispersive X-ray (EDX) elemental mapping images of Au–Cu/CNFs. (i) Line-scan EDX spectra of the two bimetallic Au–Cu alloy NPs. Inset in (i) is the corresponding Au–Cu alloy NPs. The mass ratio of Au and Cu is 1:2.

processes of the catalysts are still relatively inferior and sluggish, when compared with commercial Pt/C catalysts. Therefore, there is still a challenge to improve the HER performance of Cu-based materials fundamentally. To date, due to the corrosion and instability in acidic solutions, Cu and its complexes have rarely been used as HER catalysts.

Multimetallic nanoparticles (NPs), either heteronanostructures or homogeneous alloys, provide a versatile pathway to deliberately tailor the geometries and thereby fine-tune the electrocatalytic activity of the NPs. The previously reported Cu-based alloy, such as Au–Cu alloy are mainly homogeneous alloys and they were usually synthesized through the wet chemical methods in solution.^{20–22} Inspired by our group's previous work about the Co_9S_8 and MoS_2 core–shell CNFs electrocatalysts,¹² we provide a new strategy for the first design of bimetallic Au–Cu alloys nanoparticles with a homogeneous Au–Cu alloy phase as core and Cu phase as shell, forming a core–shell nanostructures with abundant nanointerfaces and further improving the electrochemical performance.

In the present investigation, the precursor of $\text{HAuCl}_4 \cdot 4\text{H}_2\text{O}$ and CuCl_2 were first dissolved in a nontoxic poly(vinyl alcohol) (PVA) solution. Then, the obtained precursor solution was electrospun into nanofiber membranes through the electrospinning technology. After that, the electrospun nanofiber mats were converted into CNFs with bimetallic Au–Cu alloy nanoparticles through the graphitization process in a home-built chemical vapor deposition (CVD) furnace. The CNFs with 3D architectures not only improve the charge transport but also serve as reaction vessels to bring up and protect the bimetallic alloy metal NPs from oxidation and corrosion. In addition, the CNFs can also facilitate the dispersion of alloy NPs, hindering their agglomeration at high temperatures. The

morphology, structure, and composition can be controlled by adjusting the precursor nanofibers through a green and environmentally friendly approach. The synthesized Au–Cu/CNFs membrane were directly employed as electrodes in HER. The self-supported Au–Cu/CNFs (mass ratio of Au and Cu is 1:2) membrane exhibit excellent HER performance and outstanding durability with low overpotential of 83 mV (at $j = 10 \text{ mA cm}^{-2}$), high exchange current density (0.790 mA cm^{-2}), small Tafel slope (70 mV dec^{-1}), and good stability, which are much better than the previously reported Au-based and Cu-based materials.^{23,24} The new strategy for the synthesis of bimetallic structure of Au–Cu could lead to the design of new electrocatalysts.

EXPERIMENTAL METHODS

Chemicals and Materials. Chloroauric acid ($\text{HAuCl}_4 \cdot 4\text{H}_2\text{O}$, 99.9%) and sulfuric acid were commercially available from Shanghai Civi Chemical Technology Co., Ltd. Copper chloride (CuCl_2), poly(vinyl alcohol) powder (PVA, 88% hydrolyzed, $M_w = 88000$), and epigallocatechin gallate (EGCG, 98%) were purchased from the XuanChengBaiCao Plant Industry and Trade Co., Ltd. Ultrapure water (Milli-Q) was used for all solution preparations. All of the chemicals were used without further purification.

Preparation of the Au–Cu Precursor PVA Nanofiber Membranes. In a typical procedure, 1.5 g of PVA powder was dissolved in 11 mL of ultrapure water (Milli-Q) to form a homogeneous solution under constant stirring for several hours at 80°C . Then, the $\text{HAuCl}_4 \cdot 4\text{H}_2\text{O}$ was added into the PVA solution, and the solution was magnetically stirred until the mixture became homogeneous. Next, 0.025 g of EGCG was added into the solution at 65°C . Finally, the CuCl_2 (the total mass of the metal salt was 0.075 g) was added into the above solution 30 min later. When the above mixture became stable, the precursor solution was obtained. Subsequently, the precursor solution was transferred into a syringe

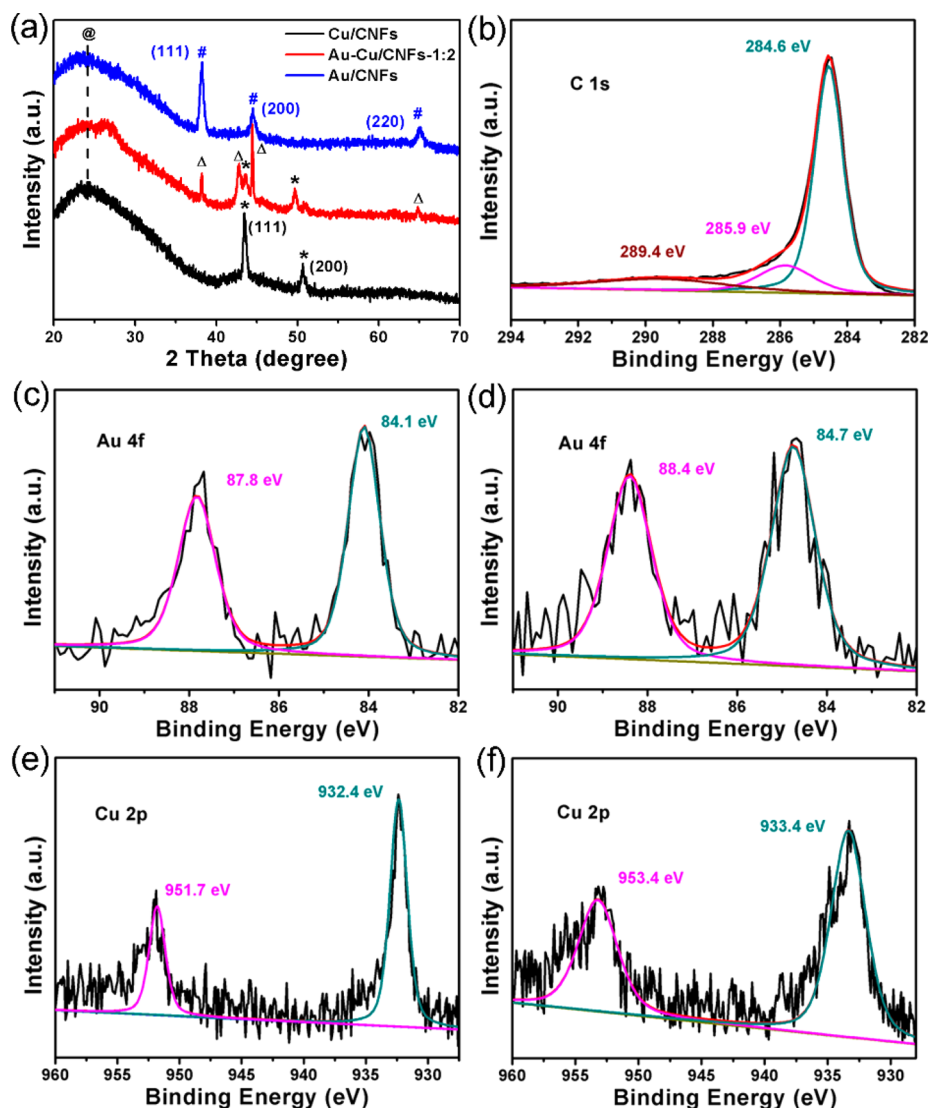


Figure 2. (a) XRD patterns of the Au/CNFs, Au–Cu/CNFs, and Cu/CNFs. (b) The C 1s XPS spectra of the Au–Cu/CNFs. The Au 4f XPS spectra of the (c) Au/CNFs and (d) Au–Cu/CNFs. The Cu 2p XPS spectra of the (e) Cu/CNFs and (f) Au–Cu/CNFs. The mass ratio of Au and Cu is 1:2.

with a capacity of 10 mL and an inner diameter of 0.8 mm. The positive voltage connected with the tip of the syringe was approximately 12 kV, the negative voltage connected with the rotating drum was approximately 1.5 kV, and the distance from the tip to the rotating drum was 12 cm. The feeding rate of the precursor solution was 0.3 mL h⁻¹, and the ambient temperature was 25 °C ± 2 °C. To remove the residual solvent, the Au–Cu precursor PVA nanofiber membranes were placed into a drying oven.

Fabrication of the Bimetallic Au–Cu/CNFs Self-Supported Electrode Materials. The bimetallic Au–Cu/CNFs self-supported electrodes were fabricated by a CVD system. The samples were heated to 230 °C and maintained for 1 h under air condition for the intramolecular dehydration reaction. Then, the samples were kept at 900 °C for 3 h in an Ar atmosphere to sufficiently graphitize the PVA nanofibers into carbon nanofibers. Subsequently, the obtained Au–Cu/CNFs were cooled to ambient temperature in the CVD furnace. During the carbonization process, the heating rate was 5 °C min⁻¹ throughout the experiment. The Au–Cu/CNF electrodes were stored in a vacuum-dried glass dish in sealed polyethylene bags until further characterization. In addition, the Au–Cu/CNF electrodes with different mass ratios of HAuCl₄·4H₂O to CuCl₂ were labeled as 2:1, 1:1, 1:2, 1:3, and 1:4, respectively. The pure Au/CNFs and the Cu/CNFs were prepared with the same conditions as the control.

Characterizations. The morphological features and the surface structures of the bimetallic Au–Cu/CNFs were obtained with a field-emission scanning electron microscope (JSM-6700F, JEOL, Japan) at an acceleration voltage of 3 kV and a transmission electron microscope (TEM) (JSM-2100, JEOL, Japan) at an acceleration voltage of 200 kV. The surface chemical compositions of the electrodes were measured by an X-ray photoelectron spectrometer (XPS) (Kratos Axis Ultra DLD) with an aluminum (mono) K α source (1486.6 eV). In addition, the crystal structures of the electrodes were characterized with a SIEMENS Diffraktometer D5000 X-ray diffractometer (XRD) using a Cu K α radiation ($\lambda = 1.5406$ Å) source at 35 kV and a scan rate of 0.02° 2 θ s⁻¹ in the 2 θ range of 20–60°. High-angle annular dark field scanning TEM (HAADF-STEM) images and STEM mapping were collected by an STEM (Tecnai G2 F30 S-Twin, Philips-FEI) at an acceleration voltage of 300 kV.

Electrochemical Measurements. All electrochemical experiments were carried out using IVIUM electrochemical workstation (Ivium Technologies BV Company, Netherlands) with a standard three-electrode cell testing system at room temperature. The hydrogen evolution reaction activity of the as-prepared electrodes was tested in 0.5 M H₂SO₄ using pure nitrogen deaerated for 30 min to remove the dissolved oxygen before each experiment. The as-prepared Au–Cu/CNFs electrodes, a graphite rod, and a saturated calomel electrode

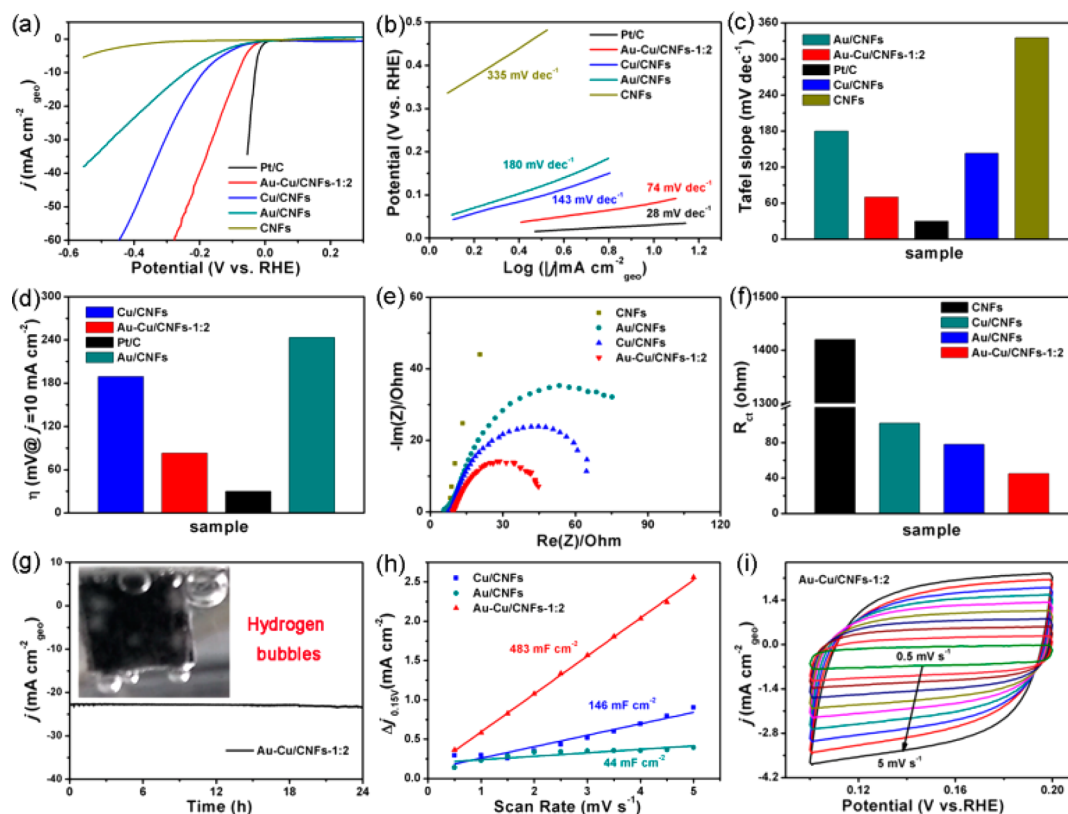


Figure 3. Electrocatalytic activity of HER with commercial Pt/C, Au–Cu/CNFs, Au/CNFs, Cu/CNFs, and CNFs catalysts obtained from a N_2 purged 0.5 M H_2SO_4 electrolyte. (a) Linear sweep voltammetry (LSV) and the corresponding (b) Tafel slopes of all the samples. (c) Histograms of Tafel slope from (b). (d) Histograms of overpotentials at $j = 10 \text{ mA cm}^{-2}$ for different samples. (e) Nyquist plots of as-prepared catalysts and the corresponding (f) histograms of R_{ct} . (g) Current–time plot of the Au–Cu/CNFs membrane under a constant applied potential of -0.136 V vs RHE. Inset in (g) is the photograph of the Au–Cu/CNFs electrode with generated H_2 bubbles. (h) The linear fit of the capacitive currents of the catalysts vs the scan rates and (i) the electrochemical cyclic voltammograms of Au–Cu/CNFs at potential scanning rates from 0.5 to 5 mV s^{-1} .

were used as the working electrodes, the counter electrode, and the reference electrode, respectively. Linear sweep voltammetry (LSV) curves, electrochemical impedance spectra (EIS), and time-dependent current density (i - t) curves were collected after 400 cycles of cyclic voltammograms (CVs) at a scan rate of 100 mV s^{-1} . In addition, the scan rate of the LSV curves was 2 mV s^{-1} , the frequencies used to obtain the EIS ranged from 100 kHz to 0.001 Hz , and the constant voltage of the i - t curves was -0.136 V vs RHE for 24 h.

RESULTS AND DISCUSSION

The morphologies and structures of the obtained Cu/CNFs, Au/CNFs, and bimetallic Au–Cu/CNFs membrane are shown in Figure 1. From Figure 1 (panels a and d), a large number of Cu NPs were densely grown on the surface of the CNFs. The Cu/CNFs exhibit distinct nanofiber morphology and integrated networks, forming the 3D architectures. The size of the Cu NPs ranges from 10 to 30 nm, as shown in Figure 1d. HRTEM images of the Cu/CNFs in Figure 1d clearly exhibit the lattice fringes of 2.1 and 1.8 Å, corresponding to the (111) and (200) planes of the metallic state of Cu NPs. Compared with the Cu/CNFs, relatively fewer Au NPs were obtained on the surfaces of CNFs due to the small amount of Au precursor (a half of the amount of Cu), and the size of Au NPs range from 5 to 20 nm (Figure 1, panels b and e). As shown in Figure 1e, the Au NPs displays a d -spacing of 2.3 Å, corresponding to the (111) plane of the Au NPs. When the Au meets Cu (the mass ratio of Au and Cu is 1:2) in the CNFs, as shown in c and f, numerous small and uniform Au–Cu alloy NPs were homogeneously and densely germinated throughout the whole CNFs. The size of

the Au–Cu alloy ranges from 10 to 20 nm and there are no obvious aggregates particles, as shown in Figure 1c.

The TEM image in Figure 1f clearly indicate that there are two kinds of contrast about the Au–Cu alloy, suggesting the side-by-side conjoined structures. The HRTEM image of the Au–Cu NPs in CNFs (inset in Figure 1f) illustrate that there are two crystal grains in Au–Cu alloy with lattice distances of 2.2 and 1.9 Å, which are attributing to the (111) plane of Au and (200) plane of Cu, respectively. The Au–Cu alloy NPs are surrounded by several carbon shells, and the labeled lattice distance of 3.6 Å is attributed to the (002) plane of graphite carbon, leading to the formation of a special “core-shell” structures (inset in Figure 1f). The carbon shell can protect the Au–Cu alloy from the oxidation and corrosion during the HER process. The HAADF-STEM image in Figure 1g also clearly demonstrates the conjoined bimetallic Au–Cu alloy. From the STEM-EDX mapping images in Figure 1h, the Au element was encapsulated in the Cu elements. It seems like the bimetallic Au–Cu alloy NPs are core–shell structures with Au phase as cores and the Cu phase as the shell. However, when the Au element area was compared with the Cu area, it is indicated that the Cu elements exist in the Au area, suggesting the formation of a homogeneous Au–Cu alloy. In order to further characterize the structures of bimetallic Au–Cu alloy NPs, the line scan EDX spectra of two Au–Cu NPs was shown in Figure 1i. From the line scan EDX spectra, the sizes of the homogeneous Au element area in two NPs are about 3.5 and 2.8 nm, while the size of Cu element area in two NPs are about

4.5 and 4.7 nm, respectively. The results indicate that the coexistence of Au and Cu elements belong to the homogeneous Au–Cu alloy phase and the enlarged Cu elements area exceeded Au elements belong to the Cu shell phase. Therefore, the structure of the bimetallic Au–Cu alloys NPs both consist of homogeneous Au–Cu alloy phase as core and Cu phase as shell, forming a “core-shell” nanostructures.

Figure 2a shows the X-ray diffraction (XRD) patterns of Au/CNFs, Cu/CNFs, and Au–Cu/CNFs-1:2. Obviously, the broad bands around 24.1° are indexed to the (002) planes of graphitic carbon (JCPDS: 26-1076) in all samples. The three peaks of the Au/CNFs are located at 38.2° , 44.5° , and 65.1° , which are indexed to the (111), (200), and (220) planes of the Au crystal (marked as #, JCPDS no. 04-0784).^{25,26} Meanwhile, the two peaks of the Cu/CNFs emerged at 43.6° and 50.7° , which are ascribed to the (111) and (200) planes of Cu crystals (marked as *, JCPDS no. 04-8036), respectively. The bimetallic Au–Cu/CNFs exhibit six distinct peaks with a broad band and five relative sharp peaks. The diffraction peaks located at 38.1° , 41.9° , 44.2° , and 64.5° are ascribed to the (111), (200), and (220) planes of the Au_3Cu alloy phase (marked as Δ , JCPDS no. 34-1302).^{27–29} The other peaks located at 44.4° and 50.2° correspond to the (111) and (200) planes of the Cu phase (marked as *, JCPDS no. 04-8036), suggesting the existence of the Cu crystals. The XRD results indicate that two crystal phases coexist in the bimetallic Au–Cu NPs including inner homogeneous Au–Cu alloy phases and outer Cu shell, which are associated with the TEM and STEM results.

XPS was employed to further analyze the surface chemical states of the Cu/CNFs, Au/CNFs, and Au–Cu/CNFs alloys. Generally, the XPS spectra further testify the presence of Au and Cu elements in the sample. In Figure 2b, the C 1s XPS spectrum of bimetallic Au–Cu/CNFs was deconvoluted into three different peaks, and the main peak is located at 284.6 eV, indicating that the primary carbon of CNF is graphite carbon.³⁰ As shown in Figure 2c, the Au 4f XPS spectrum of Au/CNFs exhibits two peaks with binding energies (BEs) at 87.8 and 84.1 eV, which are ascribed to the Au $4f_{7/2}$ and Au $4f_{5/2}$, respectively.³¹ Focusing on the Cu 2p XPS spectrum for the Cu/CNFs in Figure 2e, two sharp peaks with BEs at 951.7 and 932.4 eV, corresponding to the Cu $2p_{2/3}$ and Cu $2p_{1/2}$.³² For the Au–Cu/CNFs, the BEs of Cu 2p for Cu $2p_{2/3}$ and Cu $2p_{1/2}$ shift to 953.4 and 933.4 eV, while the peaks of Au 4f shift to 88.4 and 84.7 eV, due to the strong charge transfer between the Au species and Cu species as well as the surrounding carbon.³³ No obvious separate satellite peaks were observed in all of the XPS spectra, demonstrating that several carbon layers on the surface of the Au–Cu alloy NPs are effective in protecting the Cu and Au from oxidation. The shifts in Au 4f and Cu 2p in Au–Cu/CNFs when compared with the Au/CNFs and Cu/CNFs further indicate that the bimetallic Au–Cu have strong interaction between the inner Au–Cu alloy and outer Cu shell.

The electrocatalytic performance of the Cu/CNFs, Au/CNFs, and Au–Cu/CNFs are obtained in a typical three-electrode system in 0.5 M H_2SO_4 . The self-supported Au–Cu/CNFs membrane was directly used as an electrode for the measurement. In Figure 3a, the linear sweep voltammetry of the commercial Pt/C (20 wt % Pt/C), Au–Cu/CNFs, Au/CNFs, Cu/CNFs, and CNFs were examined under the same conditions. Unquestionably, the catalyst of the commercial Pt/C achieved the remarkable HER performance with the smallest overpotential and a high current density. In contrast, the CNFs showed negligible HER performance. As expected,

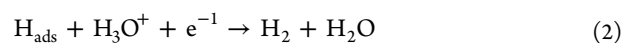
the catalyst of the Au–Cu/CNFs with a core–shell alloy structure (Au–Cu/CNFs-1:2) exhibited excellent electrochemical activity and only required a small overpotential as low as 83 mV to achieve a current density of 10 mA cm^{-2} , which is much lower than that of the most recently reported Au-based and Cu-based catalysts (Table 1). To obtain the

Table 1. Comparisons of HER Activity among Various Catalysts

samples	η @ $j = 10 \text{ mA cm}^{-2}$ (mV)	tafel slope (mV dec^{-1})	j_0 (mA cm^{-2})	C_{dl} (mF cm^{-2})
Au/CNFs	243	180	0.464	44
Au–Cu/CNFs-2:1	104	86	0.645	264
Au–Cu/CNFs-1:1	94	75	0.736	370
Au–Cu/CNFs-1:2	83	70	0.790	483
Au–Cu/CNFs-1:3	101	83	0.705	317
Au–Cu/CNFs-1:4	118	109	0.589	214
Cu/CNFs	189	143	0.496	146

current density of 10 mA cm^{-2} , the Au/CNFs and Cu/CNFs catalysts required overpotentials of 243 and 189 mV, respectively. The excellent HER activity of the Au–Cu/CNFs-1:2 could originate from the synergetic effect between the inner Au–Cu alloy and outer Cu shell.^{34,35} The bimetallic core–shell-like Au–Cu alloy possess large amounts of nano-interfaces, and the locally curved surfaces of the nanointerfaces are essentially enclosed by high densities of uncoordinated surface atoms, which serve as the active sites for catalyzing a series of interfacial chemical and electrochemical reactions.^{36–38}

Moreover, the Tafel slopes are used as a criterion for evaluating the HER mechanism. The HER involves three elementary reactions on the surface of electrodes in acidic solutions, including electrochemical hydrogen adsorption, electrochemical desorption, and chemical desorption, which are commonly referred to as the Volmer reaction (eqn 1), Heyrovsky reaction (eqn 2), and Tafel reaction (eqn 3), respectively.³⁹



As displayed in Figure 3b, the commercial Pt/C has a minimum Tafel slope of 28 mV dec^{-1} . Under the same conditions, the Tafel slopes of the Au/CNFs, Cu/CNFs, and CNFs were 143, 180, and 335 mV dec^{-1} , respectively. In addition, the Au–Cu/CNFs had a small Tafel slope of 70 mV dec^{-1} , suggesting fast kinetics and the Volmer–Heyrovsky mechanism during the HER process. To further verify the fast kinetics of the electrode in acidic environments, the Nyquist plots of the samples were also measured, as shown in Figure 3e. As expected, the semicircular diameter of the Au–Cu/CNFs was clearly smaller than that of the other catalysts. The R_{ct} of CNFs, Au/CNFs, Cu/CNFs, and Au–Cu/CNFs are 1420, 102, 78, and 45Ω , respectively. The smaller R_{ct} represents faster reaction rate and more exposed active sites on the catalysts during the HER process.⁴⁰ The stability of the Au–Cu/CNFs electrode materials is particularly important for its practical

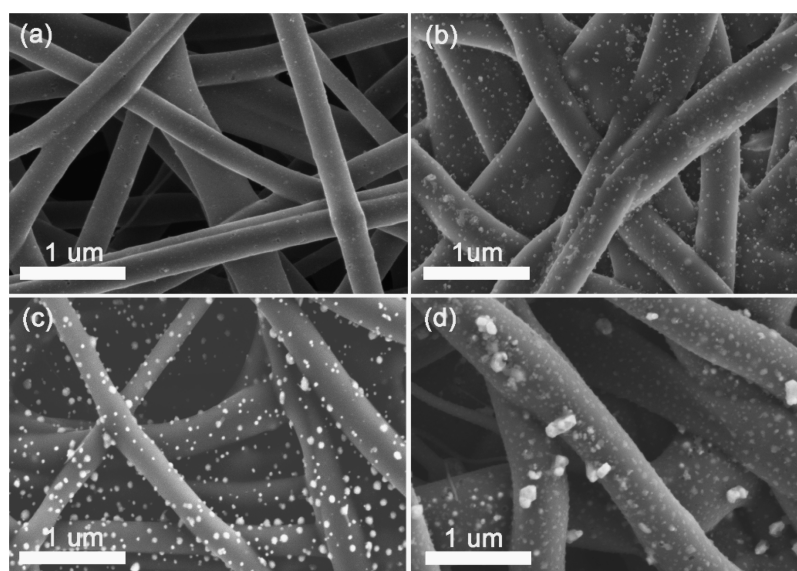


Figure 4. FE-SEM images of the (a) Au–Cu/CNFs-2:1, (b) Au–Cu/CNFs-1:1, (c) Au–Cu/CNFs-1:3, and (d) Au–Cu/CNFs-1:4.

applications, and the time-dependent current density was measured at -0.136 V versus RHE for a continuous 24 h.

As shown in Figure 3g, there was no obvious degradation in the current density after the continuous electrolysis for 24 h, indicating the exciting stability of Au–Cu/CNFs membrane. The photograph of the electrode in inset in Figure 3g clearly indicates the generation of large amounts of H_2 bubbles. Moreover, the exchange current density (j_0) values were obtained from the Tafel slopes by extrapolation, as shown in Table 1. Notably, the Au–Cu catalysts revealed the largest j_0 of $0.79 \times 10^{-3} A cm^{-2}$, which is much larger than that of the Au/CNFs ($0.464 \times 10^{-3} A cm^{-2}$) and Cu/CNFs ($0.496 \times 10^{-3} A cm^{-2}$). As we all know, a large j_0 is usually related to the electrochemically active surface area (ECSA).^{41,42} Thus, the double layer capacitance (C_{dl}) from cyclic voltammogram (CVs) curves with different scan rates was calculated as an alternative method to estimate the ECSA (Figure S1).⁴³ As shown in Figure 3h, the C_{dl} value of the Au–Cu/CNF was $483 mF cm^{-2}$ with various scan rates (from 0.5 to $5 mV s^{-1}$) when the potential range was from 0.1 to 0.2 V. The large j_0 was associated with the high ECSA, while the high surface roughness revealed more active sites and facilitated the decreasing contact between the gas bubbles and electrode.⁴⁴ Therefore, the formation/detachment of hydrogen gas bubbles on the surface of the electrode could be accelerated, leading to the fast kinetics and enhanced HER activity.

The above results indicate that the bimetallic core–shell-like Au–Cu/CNFs indeed improve the HER activity, when compared with the individual Cu/CNFs and Au/CNFs. Meanwhile, the mass ratio of Au and Cu precursor plays an essential role for the structures and morphologies of bimetallic Au–Cu and the corresponding HER activity. Therefore, we further explored the influences of the different mass ratios of $H AuCl_4 \cdot 4H_2O$ and $CuCl_2$ on the morphology and HER performance of the catalysts. Figure 4 shows the FE-SEM images of bimetallic Au–Cu alloy with different mass ratios of 2:1, 1:1, 1:3, and 1:4. As shown in Figure 4, with the increased Cu content in Au–Cu alloy, the size of the Au–Cu NPs became larger. The above results in Figure 1 have already indicated that the Cu NPs on Cu/CNF is larger than the Au NPs in Au/CNF. Figure 4d shows the morphology of the Au–

Cu/CNFs-1:4 with mass ratio of 1:4, and there are some aggregated Au–Cu alloy NPs. However, with increased Au content, as shown in Figure 4 (panels d to a), the size of the Au–Cu alloy NPs decrease gradually and there are no obvious aggregated NPs on the CNF. It is demonstrated that the introduction of Au NPs into the Au–Cu alloy can indeed decrease the size of Cu NPs, leading to the formation of Au–Cu alloy with uniform sizes.

The XRD patterns of the series of the Au–Cu/CNFs hybrid provide more information about the morphology and structure evolutions caused by the different mass ratios of Au and Cu. As shown in Figure 5, all of the samples exhibit a broad band,

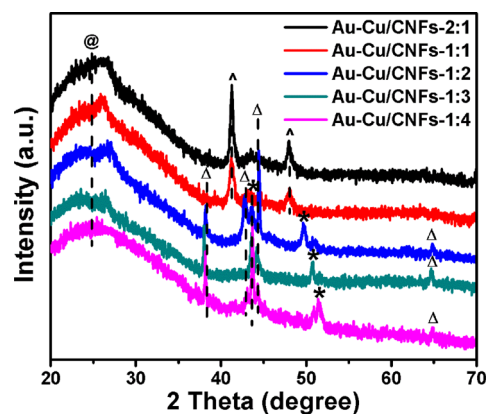


Figure 5. XRD patterns of the Au–Cu/CNFs-2:1, Au–Cu/CNFs-1:1, Au–Cu/CNFs-1:2, Au–Cu/CNFs-1:3, and Au–Cu/CNFs-1:4.

corresponding to the (002) planes of graphitic carbon (marked as @, JCPDS: 26-1076). With the increased Cu contents in Au–Cu alloys, it is interesting that there are some crystal phase transition in the Au–Cu alloy NPs. The Au–Cu/CNFs-2:1 sample exhibits two main sharp peaks located at 41.7° and 48.5° , which are indexed as the (111) and (200) planes of the $AuCu_3$ alloy phase (marked as ^, JCPDS: 35-1357).^{27–29} The XRD results demonstrate that the Au atoms enter into the unit cell of Cu atoms, leading to the successful formation of Au–Cu alloy not the mixture of Au and Cu NPs.

With the increased Cu content, the Au–Cu/CNFs-1:1 sample also exhibits two diffraction peaks, indicating that at the mass ratio of 1:1 for Au:Cu, the Au–Cu alloy NPs are still AuCu₃ phase. When the mass ratio increased to 1:2, slight peak asymmetry could suggest a range of alloy compositions in the samples. It is interesting that the Au–Cu/CNFs-1:2 demonstrate the coexistence of Au₃Cu alloy phase (diffraction peaks marked as Δ) and Cu phase, which are accordingly with the XRD results in Figure 2a. With the increased Cu contents, the former AuCu₃ alloy transforms into a Au₃Cu alloy, and there is a preferential diffusion of Cu atoms to one side of the Au₃Cu alloy NPs, forming the Cu shell. The (111) planes of AuCu₃ in Au–Cu/CNFs-2:1 and Au–Cu/CNFs-1:1 emerged at 41.7°, while the (111) planes of Au₃Cu in Au–Cu/CNFs-1:2, Au–Cu/CNFs-1:3, and Au–Cu/CNFs-1:4 emerged at 38.1°. It is reported that as more Cu is incorporated into the Au_{1-x}Cu_x crystal, the (111) peaks clearly shift to higher 2θ degree and this shift is consistent with the alloying of Au and Cu.^{45,46} The XRD results demonstrate that with the increased Cu contents, the formed Au–Cu alloy in CNFs have transformed from the AuCu₃ alloy phase to the Au₃Cu alloy phase with a Cu shell, suggesting the dealloying phenomena from AuCu₃.

In order to further investigate the morphologies evolutions of the Au–Cu alloys with different mass ratios, the HAADF-STEM and STEM-EDS mapping images are shown in Figure 6.

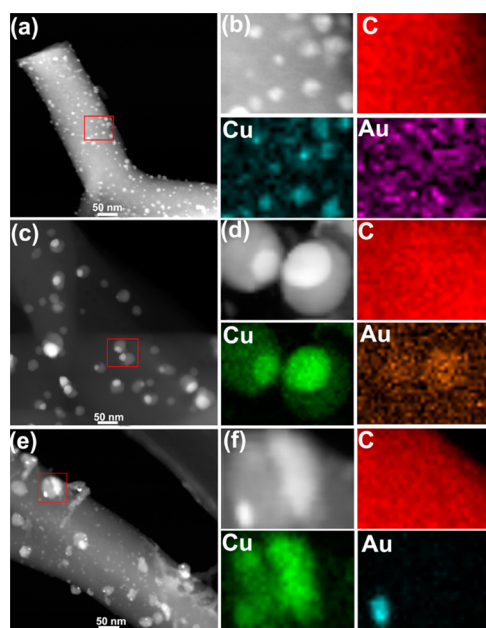


Figure 6. HAADF-STEM and STEM-EDS mapping images of the (a and b) Au–Cu/CNFs-2:1, (c and d) Au–Cu/CNFs-1:3, and (e and f) Au–Cu/CNFs-1:4.

As shown in Figure 6 (panels a and b), the Au–Cu/CNFs-2:1 exhibit small sized and uniformly Au–Cu alloys NPs in CNFs, which are associated with Figure 4a. In the mapping area, the Au and Cu elements have similar distribution areas, indicating the homogeneous AuCu₃ alloy phases. In Figure 6 (panels c and d), the Au–Cu/CNFs-1:3 display another morphology of the Au–Cu alloys, which are similar to the Au–Cu/CNFs-1:2 (Figure 1). The Cu elements distributed throughout the two Au–Cu alloy NPs, and meanwhile, the intensity of the Cu element is strong at one side of the Au–Cu alloy NPs. The Au elements signals are mainly distributed at one side of the Au–

Cu NPs, which are the same areas of the Cu elements with strong Cu signals. Notably, as shown in Figure 1 (panels e and f), the STEM-EDS mapping images of Au–Cu/CNFs-1:4 also indicate a “core-shell” Au–Cu alloy with the Au–Cu alloy phase as the core and the Cu phase as the shell. With the increased Cu contents, the size of the Au–Cu alloy increased, as well as the phase transitions from homogeneous AuCu₃ alloy to Au₃Cu–Cu “core-shell” alloy. The morphology evolutions are associated with the XRD results.

It is an interesting phenomenon that the phase transition of Au–Cu alloy and Cu dealloying in Au–Cu alloy. On the basis of the results, a feasible reason has been proposed. At a high temperature (CVD process) of 1000 °C, it is a thermodynamically controlled synthesis for controlling the components of Au–Cu alloy NPs, known as phase-stabilized synthesis.^{26–29} In our experiment, the AuCu₃ alloy can be obtained at relatively low Cu contents, while the Au₃Cu can be obtained even when the Cu contents are excessive. It is reported that the stability of Au–Cu alloy decreases in the order of AuCu₃ < AuCu < Au₃Cu.²⁶ Therefore, when the Cu contents are excessive, the former AuCu₃ alloy tend to transform into Au₃Cu alloy due to the relative higher stability of Au₃Cu alloy. The Cu contents in the AuCu₃ alloy are higher than those in the Au₃Cu alloy. Keeping the Au contents the same in all Au–Cu samples, at the beginning of the phase transition, the Cu atoms tend to dealloy on the surfaces of the NPs from the fcc AuCu₃ phase to an alloy phase with lower free energy. With increasing Cu contents, more and more Cu atoms diffused on the dealloying sites and grew in larger-sized Cu shells, forming the Au₃Cu–Cu “core-shell” alloy NPs.

Subsequently, the electrochemical performance of the alloy catalysts with different mass ratios of HAuCl₄·4H₂O and CuCl₂ were investigated under the same conditions. As shown in Figure 7 (panels a and b), the Au–Cu/CNFs with mass ratios of 1:4 require a relative higher overpotentials of about 118 mV (denoted as η_{10}) to achieve the current density of 10 mA cm⁻². The η_{10} of other Au–Cu/CNFs with mass ratios of 1:3, 1:2, 1:1, and 2:1 are 101, 83, 94, and 104 mV, respectively. The Au NPs are inactive catalysts for HER, and interestingly, the bimetallic Au–Cu/CNFs-1:2 with small Au content possess the best HER activity than other Au–Cu/CNF with different mass ratios.

Besides the synergistic effects of the bimetallic Au–Cu alloy, the Au atom has the positive influence on the decrease of Cu NPs, leading to a more exposed active site of Cu NPs and, therefore, the enhanced HER activity. However, when the Au content is larger than the Cu NPs (Au–Cu alloy with mass ratio of 1:1 and 2:1), the HER activity of Au–Cu alloy decreases because of the inactive HER activity of Au. The Au–Cu/CNFs-1:2 obtains the best HER activity with η_{10} = 84 mV, demonstrating the best mass ratio of Au–Cu alloy is 1:2. The detailed overpotential values of the catalysts are listed in Table 1. The corresponding Tafel slopes are shown in Figure 7 (panels c and d). The Au–Cu/CNFs-1:2 catalyst shows a Tafel slope of 70 mV dec⁻¹, which is lower than that of the Au–Cu/CNFs-2:1 (86 mV dec⁻¹), Au–Cu/CNFs-1:1 (75 mV dec⁻¹), Au–Cu/CNFs-1:3 (83 mV dec⁻¹), and Au–Cu/CNFs-1:4 (109 mV dec⁻¹), implying that the rate-determining step of the HER on this catalyst is electrochemical desorption.

The j_0 of these catalysts were calculated by extrapolation and are shown in Table 1. The j_0 values of the catalysts with different mass ratios are 0.645, 0.736, 0.790, 0.705, and 0.589 mA cm⁻², respectively. The linear fits of the capacitive currents

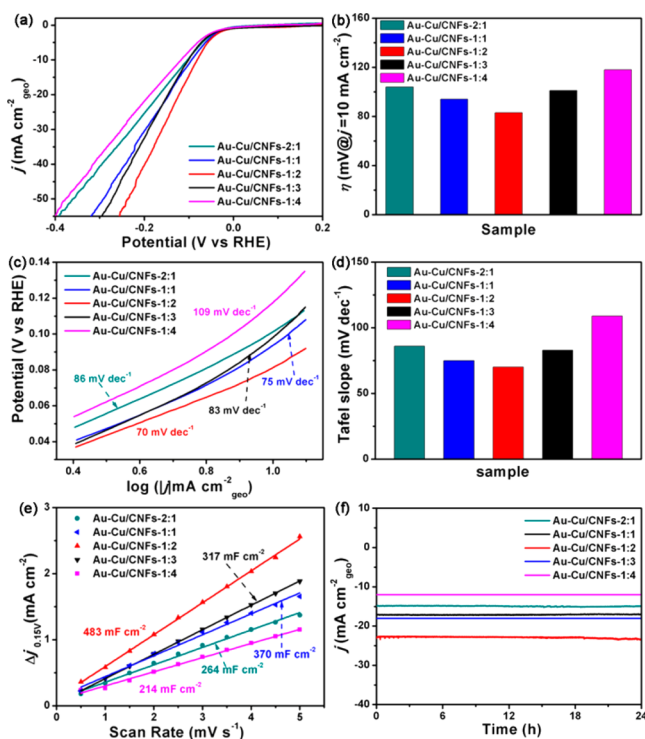


Figure 7. Electrocatalytic activity of the Au–Cu/CNFs-2:1, Au–Cu/CNFs-1:1, Au–Cu/CNFs-1:2, Au–Cu/CNFs-1:3, and Au–Cu/CNFs-1:4 catalysts for the HER in a 0.5 M H₂SO₄ solution. (a) Linear sweep voltammetry (LSV) curves and the corresponding (b) histograms of overpotential at $j = 10 \text{ mA cm}^{-2}$ for different samples. (c) Tafel slopes of all the samples and the corresponding (d) histograms. (e) The linear fit of the capacitive currents of the catalysts at different scan rates, and (f) the current–time plot of all catalysts at a constant voltage of -0.136 V vs RHE for 24 h.

are shown in Figure 7e. Compared with other catalysts, the Au–Cu/CNFs-1:2 catalyst had a larger C_{dl} value (in Table 1), which further confirms the enhanced HER activity due to the synergistic effect at the nanointerface of the Au₃Cu alloy phase and Cu shell. In addition, the mass activity and the corresponding values at -0.1 V versus RHE are shown in Figure S2 and the mass ratio of the various catalysts are summarized in Table S1, which was quantitatively determined by EDS analysis. Furthermore, the durability of all the electrode catalysts with various mass ratios are measured under a constant voltage of -0.136 V versus RHE (Figure 7f). In general, the current densities of these catalysts remain stable

even after continuous electrolysis for 24 h in acidic solution, and only a small decrease of the current density was observed, which may be due to the H₂ adsorption on the electrode surface and the depletion of H⁺ during the test process.^{47,48} Moreover, the surface morphology and crystal structures of the Au–Cu alloy remained the same, and the nanoparticles were still surrounded by several carbon shells. In addition, no obvious aggregation or detachment can be observed after HER stability test, which can be demonstrated from TEM images (Figure S3) and XRD patterns (Figure S4).

The bimetallic Au–Cu alloy with self-supported 3D architecture exhibits exciting HER activity and stability, which can directly be used as the electrode materials. There are several advantages for the enhanced HER activity of the bimetallic Au–Cu alloy: (1) the host CNFs not only serve as reaction vessels to generate the bimetallic Au₃Cu–Cu “core-shell” alloy NPs but also prevent the NPs from aggregating. (2) The bimetallic Au₃Cu–Cu “core-shell” alloy NPs possess large amounts of nanointerfaces, and the locally curved surfaces of the nanointerfaces are essentially enclosed by high densities of uncoordinated surface atoms, which serve as the active sites for catalyzing a series of interfacial chemical and electrochemical reactions. (3) The carbon layers on the surface of the NPs facilitate the charge transfer and prevent the Au–Cu NPs from oxidation and corrosion during the electrolysis. The 3D CNF architecture is beneficial to the gas desorption, therefore accelerating the kinetics of the electrode. As expected, the catalyst of the Au–Cu/CNFs with a “core-shell” alloy structure (Au–Cu/CNFs-1:2) exhibited excellent electrochemical activity and only required a small overpotential as low as 83 mV to achieve a current density of 10 mA cm^{-2} , which is much lower than that of the most recently reported Au-based and Cu-based catalysts (Table 2).

CONCLUSION

In summary, the bimetallic Au₃Cu–Cu “core-shell” alloy/CNFs have been successfully fabricated through a facile approach. The morphology, structure, and composition of bimetallic Au–Cu alloy can be controlled by adjusting the precursor in the nanofibers. With the increased Cu content, the Au–Cu alloy has a transition from the homogeneous AuCu₃ alloy phase to the Au₃Cu phase with the Cu shell. The self-supported Au–Cu/CNFs were directly employed as electrodes for HER and showed excellent electrochemical activity, including long-term stability, high exchange current density, and low overpotential. The outstanding HER performance was attributed to the synergistic effect between the Au and Cu at the nanointerfaces

Table 2. Comparisons of HER Activity with Reported Catalysts

catalysts	$\eta@j = 10 \text{ mA cm}^{-2}$ (mV)	tafel slope (mV dec ⁻¹)	j_0 (mA cm ⁻²)	ref
Au–Cu/CNFs	83	70	0.790	this work
CuMoS ₄ crystals	310	95	0.040	18
Cu ₇ S ₄ @MoS ₂	133	48	–	17
CuPdPt/C	55	25	0.070	16
CFP/NiCo ₂ O ₄ /CuS	72	41	0.246	49
CuS/Au	179	75	–	50
AuNPs@NCNRs/CNFs-16	288	93	–	51
Au@Zn–Fe–C	123	130	–	52
Au@NC	130	76.8	0.186	53
AuNPs/Ti	92.6	40	6×10^{-3}	54
Au–Pd NPs/rGO	–	29	0.47	55

with high densities of uncoordinated surface atoms and the fast kinetic for the desorption of the gas originated from the self-supported 3D architectures. The present investigations offer a new strategy for the design and synthesis of unique nanocrystals in energy conversion related application.

■ ASSOCIATED CONTENT

Supporting Information

The Supporting Information is available free of charge on the ACS Publications website at DOI: 10.1021/acsami.7b01418.

The double layer capacitance from CVs curves and the mass activity of all the samples. The TEM images of Au–Cu/CNFs-1:2 after HER stability test, the XRD pattern of Au–Cu/CNFs-1:2 before and after HER stability test, and the mass ratio of the samples (PDF)

■ AUTHOR INFORMATION

Corresponding Authors

*E-mail: zhuhanfj@zstu.edu.cn.

*E-mail: du@zstu.edu.cn.

ORCID

Han Zhu: 0000-0002-6274-852X

Notes

The authors declare no competing financial interest.

■ ACKNOWLEDGMENTS

This study was supported by the National Natural Science Foundation of China (NSFC) (Grants 51373154 and 51573166), the MOE & SAFEA, and 111 Project (B13025).

■ REFERENCES

- (1) Anantharaj, S.; Ede, S. R.; Sakthikumar, K.; Karthick, K.; Mishra, S.; Kundu, S. Recent Trends and Perspectives in Electrochemical Water Splitting with an Emphasis on Sulfide, Selenide, and Phosphide Catalysts of Fe, Co, and Ni: A Review. *ACS Catal.* **2016**, *6*, 8069–8097.
- (2) Turner, J. A. Sustainable Hydrogen Production. *Science* **2004**, *305*, 972–974.
- (3) Lv, H.; Xi, Z.; Chen, Z.; Guo, S.; Yu, Y.; Zhu, W.; Li, Q.; Zhang, X.; Pan, M.; Lu, G.; Mu, S.; Sun, S. A New Core/Shell NiAu/Au Nanoparticle Catalyst with Pt-Like Activity for Hydrogen Evolution Reaction. *J. Am. Chem. Soc.* **2015**, *137*, 5859–5862.
- (4) McKone, J. R.; Warren, E. L.; Bierman, M. J.; Boettcher, S. W.; Brunschwig, B. S.; Lewis, N. S.; Gray, H. B. Evaluation of Pt, Ni, and Ni-Mo Electrocatalysts for Hydrogen Evolution on Crystalline Si Electrodes. *Energy Environ. Sci.* **2011**, *4*, 3573–3583.
- (5) Shen, Y.; Lua, A. C.; Xi, J.; Qiu, X. Ternary Platinum-Copper-Nickel Nanoparticles Anchored to Hierarchical Carbon Supports as Free-Standing Hydrogen Evolution Electrodes. *ACS Appl. Mater. Interfaces* **2016**, *8*, 3464–3472.
- (6) Shao, F. Q.; Lin, X. X.; Feng, J. J.; Yuan, J.; Chen, J. R.; Wang, A. J. Simple Fabrication of Core-Shell AuPt@Pt Nanocrystals Supported on Reduced Graphene Oxide for Ethylene Glycol Oxidation and Hydrogen Evolution Reactions. *Electrochim. Acta* **2016**, *219*, 321–329.
- (7) Liu, Y. R.; Gou, J. X.; Li, X.; Dong, B.; Han, G. Q.; Hu, W.; Shang, X.; Chai, Y.; Liu, Y.; Liu, C. Self-Sacrificial Template Method of $\text{Mo}_3\text{O}_{10}(\text{C}_6\text{H}_8\text{N})_2 \cdot 2\text{H}_2\text{O}$ to Fabricate $\text{MoS}_2/\text{Carbon-Doped MoO}_2$ Nanobelts as Efficient Electrocatalysts for Hydrogen Evolution Reaction. *Electrochim. Acta* **2016**, *216*, 397–404.
- (8) Zhou, H.; Yu, F.; Sun, J.; Zhu, H.; Mishra, I. K.; Chen, S.; Ren, Z. Highly Efficient Hydrogen Evolution from Edge-Oriented $\text{WS}_2(1-x)\text{-Se}_{2x}$ Particles on Three-Dimensional Porous NiSe_2 Foam. *Nano Lett.* **2016**, *16*, 7604–7609.
- (9) Liang, H. W.; Brüller, S.; Dong, R.; Zhang, J.; Feng, X.; Müllen, K. Molecular Metal- N_x Centres in Porous Carbon for Electrocatalytic Hydrogen Evolution. *Nat. Commun.* **2015**, *6*, 7992–7992.
- (10) Yin, J.; Fan, Q.; Li, Y.; Cheng, F.; Zhou, P.; Xi, P.; Sun, S. Ni-C-N Nanosheets as Catalyst for Hydrogen Evolution Reaction. *J. Am. Chem. Soc.* **2016**, *138*, 14546–14549.
- (11) Zhu, H.; Zhang, J.; Yanzhang, R.; Du, M.; Wang, Q.; Gao, G.; Wu, G.; Zhang, M.; Liu, B.; Yao, J.; et al. When Cubic Cobalt Sulfide Meets Layered Molybdenum Disulfide: A Core-Shell System Toward Synergetic Electrocatalytic Water Splitting. *Adv. Mater.* **2015**, *27*, 4752–4759.
- (12) Kong, D.; Wang, H.; Lu, Z.; Cui, Y. CoSe_2 Nanoparticles Grown on Carbon Fiber Paper: An Efficient and Stable Electrocatalyst for Hydrogen Evolution Reaction. *J. Am. Chem. Soc.* **2014**, *136*, 4897–4900.
- (13) Han, S.; Hong, S.; Ham, J.; Yeo, J.; Lee, J.; Kang, B.; Lee, P.; Kwon, J.; Lee, S. S.; Ko, S. H.; et al. Flexible Electronics: Fast Plasmonic Laser Nanowelding for a Cu-Nanowire Percolation Network for Flexible Transparent Conductors and Stretchable Electronics. *Adv. Mater.* **2014**, *26*, 5808–5814.
- (14) Gawande, M. B.; Goswami, A.; Felpin, F. X.; Asefa, T.; Huang, X.; Silva, R.; Zou, X.; Zboril, R.; Varma, R. S. Cu and Cu-Based Nanoparticles: Synthesis and Applications in Catalysis. *Chem. Rev.* **2016**, *116*, 3722–3811.
- (15) Ahn, Y.; Jeong, Y.; Lee, D.; Lee, Y. Copper Nanowire-Graphene Core-Shell Nanostructure for Highly Stable Transparent Conducting Electrodes. *ACS Nano* **2015**, *9*, 3125–3133.
- (16) Ding, T.; Wang, Z.; Zhang, L.; Wang, C.; Sun, Y.; Yang, Q. A Highly Active and Durable CuPdPt/C Electrocatalyst for An Efficient Hydrogen Evolution Reaction. *J. Mater. Chem. A* **2016**, *4*, 15309–15315.
- (17) Xu, J.; Cui, J.; Guo, C.; Zhao, Z.; Jiang, R.; Xu, S.; Zhuang, Z.; Huang, Y.; Wang, L.; Li, Y. Ultra small $\text{Cu}_7\text{S}_4/\text{MoS}_2$ Hetero-Nanoframes with Abundant Active Edge Sites for Ultrahigh-Performance Hydrogen Evolution. *Angew. Chem.* **2016**, *128*, 6612–6615.
- (18) Tran, P. D.; Nguyen, M.; Pramana, S. S.; Bhattacharjee, A.; Chiam, S. Y.; Fize, J.; Field, M. J.; Artero, V.; Wong, L. H.; Barber, J.; et al. Copper Molybdenum Sulfide: A New Efficient Electrocatalyst for Hydrogen Production From Water. *Energy Environ. Sci.* **2012**, *5*, 8912–8916.
- (19) Jahan, M.; Liu, Z.; Loh, K. P. A Graphene Oxide and Copper-Centered Metal Organic Framework Composite as a Tri-Functional Catalyst for HER, OER, and ORR. *Adv. Funct. Mater.* **2013**, *23*, 5363–5372.
- (20) Yoshida, Y.; Uto, K.; Hattori, M.; Tsuji, M. Synthesis and Growth Mechanism of Au@Cu Core-Shell Nanorods Having Excellent Antioxidative Properties. *CrystEngComm* **2014**, *16*, 5672–5680.
- (21) Monzó, J.; Malewski, Y.; Kortlever, R.; Vidal-Iglesias, F. J.; Solla-Gullón, J.; Koper, M. T. M.; Rodriguez, P. Enhanced Electrocatalytic Activity of Au@Cu Core@Shell Nanoparticles Towards CO_2 Reduction. *J. Mater. Chem. A* **2015**, *3*, 23690–23698.
- (22) Kuo, C. H.; Hua, T. E.; Huang, M. H. Au Nanocrystal-Directed Growth of Au-Cu₂O Core-Shell Heterostructures with Precise Morphological Control. *J. Am. Chem. Soc.* **2009**, *131*, 17871–17878.
- (23) Mi, Y.; Wen, L.; Wang, Z.; Cao, D.; Zhao, H.; Zhou, Y.; Grote, F.; Lei, Y. Ultra-low Mass Loading of Platinum Nanoparticles on Bacterial Cellulose Derived Carbon Nanofibers for Efficient Hydrogen Evolution. *Catal. Today* **2016**, *262*, 141–145.
- (24) Ozel, F.; Aslan, E.; Sarilmaz, A.; Hatay Patir, I. Hydrogen Evolution Catalyzed by Cu_2WS_4 at Liquid-Liquid Interfaces. *ACS Appl. Mater. Interfaces* **2016**, *8*, 25881–25887.
- (25) Bauer, J. C.; Mullins, D.; Li, M.; Wu, Z.; Payzant, E. A.; Overbury, S. H.; Dai, S. Synthesis of Silica Supported AuCu Nanoparticle Catalysts and the Effects of Pretreatment Conditions for the CO Oxidation Reaction. *Phys. Chem. Chem. Phys.* **2011**, *13*, 2571–2581.
- (26) Zhao, W.; Yang, L.; Yin, Y.; Jin, M. Thermodynamic Controlled Synthesis of Intermetallic Au_3Cu Alloy Nanocrystals from Cu Microparticles. *J. Mater. Chem. A* **2014**, *2*, 902–906.

- (27) Gilroy, K. D.; Ruditskiy, A.; Peng, H. C.; Qin, D.; Xia, Y. Bimetallic Nanocrystals: Syntheses, Properties, and Applications. *Chem. Rev.* **2016**, *116*, 10414–10472.
- (28) Thota, S.; Chen, S.; Zhao, J. An Unconventional Mechanism of Hollow Nanorod Formation: Asymmetric Cu Diffusion in Au-Cu Alloy Nanorods during Galvanic Replacement Reaction. *Chem. Commun.* **2016**, *52*, 5593–5596.
- (29) Wilson, O. M.; Scott, R. W.; Garcia-Martinez, J. C.; Crooks, R. M. Synthesis, Characterization, and Structure-Selective Extraction of 1–3-nm Diameter AuAg Dendrimer-Encapsulated Bimetallic Nanoparticles. *J. Am. Chem. Soc.* **2005**, *127*, 1015–1024.
- (30) Shervedani, R. K.; Amini, A. Sulfur-Doped Graphene as a Catalyst Support: Influences of Carbon Black and Ruthenium Nanoparticles on the Hydrogen Evolution Reaction Performance. *Carbon* **2015**, *93*, 762–773.
- (31) Zhu, H.; Du, M.; Zhang, M.; Zou, M.; Yang, T.; Wang, L.; Yao, J. M.; Guo, B. Probing the Unexpected Behavior of Au NPs Migrating Through Nanofibers: A New Strategy for the Fabrication of Carbon Nanofiber-Noble Metal Nanocrystal Hybrid Nanostructures. *J. Mater. Chem. A* **2014**, *2*, 11728–11741.
- (32) Li, F.; Li, J.; Lin, X.; Li, X.; Fang, Y.; Jiao, L.; An, X.; Fu, Y.; Jin, J.; Li, R. Designed Synthesis of Multi-Walled Carbon Nanotubes@Cu@MoS₂ Hybrid as Advanced Electrocatalyst for Highly Efficient Hydrogen Evolution Reaction. *J. Power Sources* **2015**, *300*, 301–308.
- (33) Duan, J.; Chen, S.; Dai, S.; Qiao, S. Z. Shape Control of Mn₃O₄ Nanoparticles on Nitrogen-Doped Graphene for Enhanced Oxygen Reduction Activity. *Adv. Funct. Mater.* **2014**, *24*, 2072–2078.
- (34) Wang, P.; Jiang, K.; Wang, G.; Yao, J.; Huang, X. Phase and Interface Engineering of Platinum-Nickel Nanowires for Efficient Electrochemical Hydrogen Evolution. *Angew. Chem.* **2016**, *128*, 13051–13055.
- (35) Sun, X.; Li, D.; Ding, Y.; Zhu, W.; Guo, S.; Wang, Z. L.; Sun, S. Core/shell Au/CuPt Nanoparticles and Their Dual Electrocatalysis for Both Reduction and Oxidation Reactions. *J. Am. Chem. Soc.* **2014**, *136*, 5745–5749.
- (36) Lazzeri, M.; Vittadini, A.; Selloni, A. Structure and Energetics of Stoichiometric TiO₂ Anatase Surfaces. *Phys. Rev. B: Condens. Matter Mater. Phys.* **2001**, *63*, 155401–155409.
- (37) Li, G. G.; Lin, Y.; Wang, H. Residual Silver Remarkably Enhances Electrocatalytic Activity and Durability of Dealloyed Gold Nanosponge Particles. *Nano Lett.* **2016**, *16*, 7248–7253.
- (38) Price, S. W.; Speed, J. D.; Kannan, P.; Russell, A. E. Exploring the First Steps in Core-Shell Electrocatalyst Preparation: In Situ Characterization of the Underpotential Deposition of Cu on Supported Au Nanoparticles. *J. Am. Chem. Soc.* **2011**, *133*, 19448–19458.
- (39) Li, Y. G.; Wang, H. L.; Xie, L. M.; Liang, Y. Y.; Hong, G. S.; Dai, H. J. MoS₂ Nanoparticles Grown in Graphene: An Advanced Catalyst for the Hydrogen Evolution Reaction. *J. Am. Chem. Soc.* **2011**, *133*, 7296–7299.
- (40) Wang, S.; Wang, J.; Zhu, M.; Bao, X.; Xiao, B.; Su, D.; Li, H.; Wang, Y. Molybdenum-Carbide-Modified Nitrogen-Doped Carbon Vesicle Encapsulating Nickel Nanoparticles: A Highly Efficient, Low-Cost Catalyst for Hydrogen Evolution Reaction. *J. Am. Chem. Soc.* **2015**, *137*, 15753–15759.
- (41) Pu, Z.; Saana Amiin, I.; Wang, M.; Yang, Y.; Mu, S. Semimetallic MoP₂: An Active and Stable Hydrogen Evolution Electrocatalyst Over the Whole pH Range. *Nanoscale* **2016**, *8*, 8500–8504.
- (42) Trasatti, S.; Petrii, O. A. Real Surface Area Measurements in Electrochemistry. *J. Electroanal. Chem.* **1992**, *327*, 353–376.
- (43) McCrory, C. C.; Jung, S.; Peters, J. C.; Jaramillo, T. F. Benchmarking Heterogeneous Electrocatalysts for the Oxygen Evolution Reaction. *J. Am. Chem. Soc.* **2013**, *135*, 16977–16987.
- (44) Li, Y.; Zhang, H.; Xu, T.; Lu, Z.; Wu, X.; Wan, P.; Sun, X.; Jiang, L. Under-Water Superaerophobic Pine-Shaped Pt Nanoarray Electrode for Ultrahigh-Performance Hydrogen Evolution. *Adv. Funct. Mater.* **2015**, *25*, 1737–1744.
- (45) Motl, N. E.; Ewusiannan, E.; Sines, I. T.; Jensen, L.; Schaak, R. E. Au–Cu Alloy Nanoparticles with Tunable Compositions and Plasmonic Properties: Experimental Determination of Composition and Correlation with Theory. *J. Phys. Chem. C* **2010**, *114*, 19263–19269.
- (46) Xu, Z.; Lai, E.; Shao-Horn, Y.; Hamad-Schifferli, K. Compositional dependence of the stability of AuCu alloy nanoparticles. *Chem. Commun.* **2012**, *48*, 5626–5628.
- (47) Ray, C.; Dutta, S.; Negishi, Y.; Pal, T. A New Stable Pd-Mn₃O₄ Nanocomposite as An Efficient Electrocatalyst for the Hydrogen Evolution Reaction. *Chem. Commun.* **2016**, *52*, 6095–6098.
- (48) Yang, Y.; Fei, H.; Ruan, G.; Tour, J. M. Porous Cobalt-Based Thin Film as a Bifunctional Catalyst for Hydrogen Generation and Oxygen Generation. *Adv. Mater.* **2015**, *27*, 3175–3180.
- (49) An, L.; Huang, L.; Zhou, P.; Yin, J.; Liu, H.; Xi, P. A Self-Standing High-Performance Hydrogen Evolution Electrode with Nanostructured NiCo₂O₄/CuSHeterostructures. *Adv. Funct. Mater.* **2015**, *25*, 6814–6822.
- (50) Basu, M.; Nazir, R.; Fageria, P.; Pande, S. Construction of CuS/Au Heterostructure through a Simple Photoreduction Route for Enhanced Electrochemical Hydrogen Evolution and Photocatalysis. *Sci. Rep.* **2016**, *6*, 34738.
- (51) Zhang, M.; Wang, S.; Li, T.; Chen, J.; Zhu, H.; Du, M. Nitrogen and Gold Nanoparticles Co-Doped Carbon Nanofiber Hierarchical Structures for Efficient Hydrogen Evolution Reactions. *Electrochim. Acta* **2016**, *208*, 1–9.
- (52) Lu, J.; Zhou, W.; Wang, L.; Jia, J.; Ke, Y.; Yang, L.; Zhou, K.; Liu, X.; Tang, Z.; Chen, S.; et al. Core-Shell Nanocomposites Based on Gold Nanoparticle@Zinc-Iron-Embedded Porous Carbons Derived from Metal-Organic Frameworks as Efficient Dual Catalysts for Oxygen Reduction and Hydrogen Evolution Reactions. *ACS Catal.* **2016**, *6*, 1045–1053.
- (53) Zhou, W.; Xiong, T.; Shi, C.; Zhou, J.; Zhou, K.; Zhu, N.; Li, L.; Tang, Z.; Chen, S. Bioreduction of Precious Metals by Microorganism: Efficient Gold@N-Doped Carbon Electrocatalysts for the Hydrogen Evolution Reaction. *Angew. Chem.* **2016**, *128*, 8556–8560.
- (54) Amin, M. A.; Fadlallah, S. A.; Alosaimi, G. S.; Kandemirli, F.; Saracoglu, M.; Szunerits, S.; Boukherroub, R. Cathodic Activation of Titanium-Supported Gold Nanoparticles: An Efficient and Stable Electrocatalyst for the Hydrogen Evolution Reaction. *Int. J. Hydrogen Energy* **2016**, *41*, 6326–6341.
- (55) Darabdharma, G.; Amin, M. A.; Mersal, G. A.; Ahmed, E. M.; Das, M. R.; Zakaria, M. B.; Malgras, V.; Alshehri, S. M.; Yamauchi, Y.; Szunerits, S.; Boukherroub, R. Reduced Graphene Oxide Nanosheets Decorated With Au, Pd and Au-Pd Bimetallic Nanoparticles as Highly Efficient Catalysts for Electrochemical Hydrogen Generation. *J. Mater. Chem. A* **2015**, *3*, 20254–20266.